JPE 16-6-29

http://dx.doi.org/10.6113/JPE.2016.16.6.2294
ISSN(Print): 1598-2092 / ISSN(Online): 2093-4718

Design of Emotional Learning Controllers for AC Voltage and Circulating Current of Wind-Farm-Side Modular Multilevel Converters

Keli Li*, Yong Liao†, Ren Liu*, and Jimiao Zhang*

*,†School of Electrical Engineering, Chongqing University, Chongqing, China

Abstract

The introduction of a high-voltage direct-current (HVDC) system based on a modular multilevel converter (MMC) for wind farm integration has stimulated studies on methods to control this type of converter. This research article focuses on the control of the AC voltage and circulating current for a wind-farm-side MMC (WFS-MMC). After theoretical analysis, emotional learning (EL) controllers are proposed for the controls. The EL controllers are derived from the learning mechanisms of the amygdala and orbitofrontal cortex which make the WFS-MMC insensitive to variance in system parameters, power change, and fault in the grid. The *d*-axis and *q*-axis currents are respectively considered for the *d*-axis and *q*-axis voltage controls to improve the performance of AC voltage control. The practicability of the proposed control is verified under various conditions with a point-to-point MMC-HVDC system. Simulation results show that the proposed method is superior to the traditional proportional-integral controller.

Key words: AC voltage control, Circulating current control, Emotional learning, High-voltage direct current, Modular multilevel converter, Wind power grid connection

I. INTRODUCTION

Wind power, as an alternative to burning fossil fuels, has become a significant generating source for electricity because of the ever-increasing demand for reducing greenhouse gas emissions. As of December 2014, at least 83 countries supplied total 369,553 MW wind power to grids, and an annual growth rate reached 20% [1]-[3]. Therefore, a highly reliable wind power grid connection is necessary to guarantee high-quality power supply. The faults occurring on the grid or wind farm can directly affect one another because of the connection of AC cables. Such cables also need reactive power compensation [4], [5], [13]. These disadvantages curb the development of wind power. Over the past few years, voltage source converter (VSC) high-voltage direct-current (HVDC) has proven to be a superior solution to wind power integration [6], [7]. Self-commutated semiconductors enable wind-farm-side (WFS) VSCs to independently control AC voltage and supply passive loads as well as weak grids [8]. Furthermore, modular multilevel converters (MMC) have advantages over two-level VSCs [9]. MMC capacity is flexible for expansion with the contribution of modular topology. MMC harmonics likewise decrease as the number of sub-modules increases, and thus considerably smaller or even no harmonic filter is needed for MMCs [10]-[12].

The WFS-MMC acts as an infinite AC voltage source to collect and transmit wind power to the grid via the grid-side MMC (GS-MMC). Relevant studies have been conducted on WFS converter control. Xu et al. [13] proposed an AC voltage control with only a feedback control loop via the modulation index. Lin et al. [14] presented a novel AC voltage and phase-angle control scheme for WFS converters of AC/VSC-HVDC hybrid transmission systems. The converter operates at variable frequency based on an optimum electrical frequency search algorithm, and a coordinated control between wind farm and the converter is developed. In the MMC system, modular topology and capacitor voltage variation lead to circulating currents among three phases [15]. The circulating current mainly contains second-order harmonic components [15]-[17]. Reference [15]

Manuscript received Feb. 23, 2016; accepted Jun. 21, 2016
Recommended for publication by Associate Editor Yihua Hu.
†Corresponding Author: yongliaocqu@vip.sina.com
Tel: +86-136-0839-8620, Chongqing University
*School of Electrical Engineering, Chongqing University, China

proposed a circulating current control based on a proportional-integral (PI) controller in a *dq* reference frame without affecting the output voltage and current of the MMC at the AC side. In [18], a proportional-resonant-type minor loop is incorporated to regulate the circulating current.

Randomness and difficulty of forecasting are the distinct features of wind power. These weaknesses, along with change in local load, introduce challenges to the integration of large-capacity wind power into a power system. These challenges include AC voltage stability, power quality, and effect on weak grid. Thus, a higher level of adaptability for the control of WFS-MMC is needed. The objectives of this research are to develop adaptive controllers based on emotional learning (EL) for controlling the AC voltage and circulating current of WFS-MMC, as well as to achieve high performance of WFS-MMC. EL control is a promising control strategy for AC voltage and circulating current controls because of its fast dynamic response and robustness. The learning mechanisms of the amygdala and orbitofrontal cortex shape the association between output and input [19], [20], as well as enable the EL controller to be adaptive. The organization of this article is organized as follows. Section 2 analyzes the WFS-MMC model in a synchronously rotating *dq* reference frame. Section 3 presents novel EL control structures for AC voltage and circulating current controls. Section 4 describes studies carried out via point-to-point MMC-HVDC system with a connection of a wind farm in the Power Systems Computer Aided Design environment. The section also discusses the advantages of the proposed EL controllers over the traditional PI controllers under various conditions. Finally, Section 5 concludes.

II. MATHEMATICAL MODEL

The diagram of a three-phase MMC converter and its sub-module is depicted in Fig. 1. Each arm includes N (N=80) sub-modules and a series-connected arm inductance L_A; the sub-module consists of a half-bridge cell. In the normal condition, the sub-module works in two states: inserting state with capacitor voltage (denoted by S=1, and v_{sm}=v_C, T_1 switch on, T_2 switch off) and bypassing state with zero voltage (denoted by S=0, and v_{sm}=0, T_1 switch off, T_2 switch on).

A. Mathematical Model of MMC

The voltage equations derived from the AC bus in Fig. 1 are obtained as follows:

$$\begin{cases} L_G \dfrac{di_a}{dt} = v_{sa} - v_{ta} - i_a R_G \\ L_G \dfrac{di_b}{dt} = v_{sb} - v_{tb} - i_b R_G \\ L_G \dfrac{di_c}{dt} = v_{sc} - v_{tc} - i_c R_G \end{cases} \tag{1}$$

where v_{sj} (j=a, b, c, means phases a, b, and c) is the voltage at the point of common coupling. The arm voltage is composed

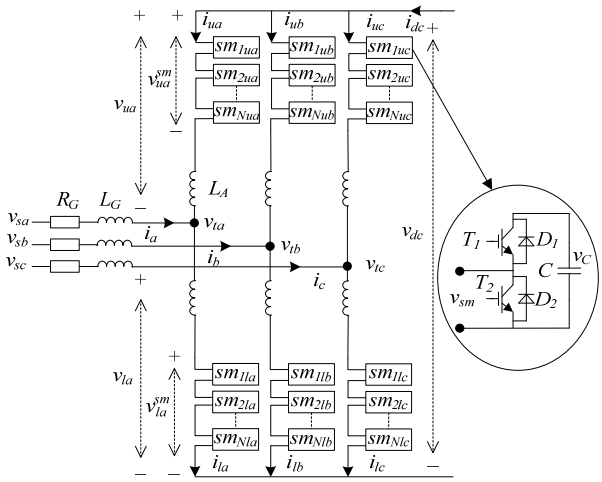

Fig. 1. MMC topology.

of the AC and DC voltages and can be represented as

$$\begin{cases} v_{uj}^{sm} = \dfrac{1}{2} v_{dc} - v_{tj} - L_A \dfrac{di_{uj}}{dt} \\ v_{lj}^{sm} = \dfrac{1}{2} v_{dc} + v_{tj} - L_A \dfrac{di_{lj}}{dt} \end{cases} \tag{2}$$

where v_{uj}^{sm} and v_{lj}^{sm} are voltages in the upper and lower arms respectively. These voltages need to be modulated. Three components exist in the upper and lower arm currents: i_{uj} and i_{lj}. The currents can be described as follows:

$$\begin{cases} i_{uj} = -\dfrac{1}{2} i_j + \dfrac{1}{3} i_{dc} + i_{cirj} \\ i_{lj} = \dfrac{1}{2} i_j + \dfrac{1}{3} i_{dc} + i_{cirj} \end{cases} \tag{3}$$

where i_{cirj} is the circulating current that flows among three phases and can be derived from Eq. (3), as shown in Eq. (4). The second-order harmonic component dominates i_{cirj}, which will augment the arm current, reduce utilization of power electronic devices, and increase capacitor voltage ripple if no circulating current control is used.

$$i_{cirj} = i_{uj} + i_{lj} - \frac{1}{3} i_{dc} \tag{4}$$

Substituting Eq. (3) into Eq. (1) yields

$$\begin{cases} v_{uj}^{sm} = \dfrac{1}{2} v_{dc} - e_j - v_{cirj} - \dfrac{1}{3} L_A \dfrac{di_{dc}}{dt} \\ v_{lj}^{sm} = \dfrac{1}{2} v_{dc} + e_j - v_{cirj} - \dfrac{1}{3} L_A \dfrac{di_{dc}}{dt} \end{cases} \tag{5}$$

where e_j and v_{cirj} denote the inner converter electromotive force (EMF) and the inner unbalance voltage respectively and can be shown as

$$e_j = v_{tj} - \frac{1}{2} L_A \frac{di_a}{dt} \tag{6}$$

$$v_{cirj} = L_A \frac{di_{cirj}}{dt} \tag{7}$$

When the effect of i_{dc} on arm voltage is disregarded, Eq. (5) can be rewritten as follows:

$$\begin{cases} v_{uj}^{sm} = \frac{1}{2}v_{dc} - e_j - v_{cirj} \\ v_{lj}^{sm} = \frac{1}{2}v_{dc} + e_j - v_{cirj} \end{cases} \quad (8)$$

Replacing v_{tj} with e_j can change Eq. (1) to

$$\begin{cases} e_a = v_{sa} - L_S\frac{di_a}{dt} - i_aR_G \\ e_b = v_{sb} - L_S\frac{di_b}{dt} - i_bR_G \\ e_c = v_{sc} - L_S\frac{di_c}{dt} - i_cR_G \end{cases} \quad (9)$$

where

$$L_S = L_G + \frac{1}{2}L_A \quad (10)$$

The AC voltage control is implemented in the synchronously rotating *dq* reference frame. Eq. (11) is the voltage equation derived by transforming Eq. (9) to the *dq* reference frame.

$$\begin{cases} e_d = v_{sd} - L_S\frac{di_d}{dt} + \omega L_S i_q - i_dR_G \\ e_q = v_{sq} - L_S\frac{di_q}{dt} - \omega L_S i_d - i_qR_G \end{cases} \quad (11)$$

where ω is the electrical frequency. Likewise, Eq. (7) can be transformed to a double line-frequency, negative-sequence rotating *dq* reference frame to obtain Eq. (12).

$$\begin{cases} v_{cird} = L_A\frac{di_{cird}}{dt} - 2\omega L_A i_{cirq} \\ v_{cirq} = L_A\frac{di_{cirq}}{dt} + 2\omega L_s i_{cird} \end{cases} \quad (12)$$

The circulating current control is designed based on Eq. (12).

B. Mathematical Model of EL

EL helps animals to avoid problems and enables them to adapt to changes in their environment. This notion inspired Moren and Balkenius [19] to develop a computational model that mimics the EL mechanism of the brain (Fig. 2). The amygdala is a structure that is responsible for the emotional evaluation of stimuli created by the sensory cortex and thalamus. The orbitofrontal cortex inhibits emotional reactions.

The final output of the EL structure, E, is composed of E_A from the amygdala and E_O from the orbitofrontal cortex, as shown in Eq. (13). The amygdala sums A_i nodes that are acquired by multiplying S_i, the stimuli from the thalamus and sensory cortex, by the plastic connection weight V_i, as shown in Eqs. (14) and (15).

$$E = E_A - E_O \quad (13)$$

$$E_A = \sum_i A_i \quad (14)$$

$$A_i = S_iV_i \quad (15)$$

The learning mechanism of the amygdala is shown below:

$$V_i = V_i + \alpha S_i \max(0, [R - \sum_j A_j]) \quad (16)$$

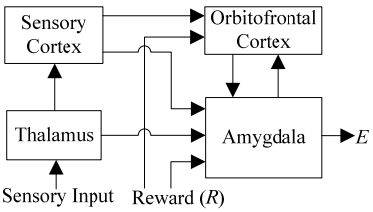

Fig. 2. EL structure.

where R is the reward function. The learning of the amygdala is permanent; V_i adjusts monotonically with learning rate α. Inhibition lies with the orbitofrontal cortex. The cortex obtains E_O by summing O_i nodes, which are the output after multiplying S_i by connection weights W_i, as shown in Eqs. (17) and (18).

$$E_O = \sum_i O_i \quad (17)$$

$$O_i = S_iW_i \quad (18)$$

However, unlike the amygdala, the learning mechanism of the orbitofrontal cortex is not monotonic and is expressed as

$$W_i = W_i + \beta R_O \quad (19)$$

where β is the learning rate, and R_O is

$$R_O = \begin{cases} \max(0, \sum_i A_i - R) - \sum_i O_i & if \ \ R \neq 0 \\ \max(0, \sum_i A_i - \sum_i O_i) & \text{otherwise} \end{cases} \quad (20)$$

The proposed EL controllers for the AC voltage and circulating current controls use the EL mechanism described above.

III. EL CONTROLLER FOR WFS-MMC

A. Control of WFS-MMC

The primary function of WFS-MMC control is to regulate AC voltage to the desired voltage amplitude and frequency, as well as provide constant AC voltage for the wind farm. The entire framework of WFS-MMC control is depicted in Fig. 3, which mainly consists of AC voltage and circulating current controls. The corresponding components are described in the following sections. Nearest-level modulation is used for the MMC modulation.

B. AC Voltage Control

Both steady and transient control performance must be evaluated for AC voltage control. The AC voltage controller can benefit from considering the dynamic factor, which has a remarkable effect on AC voltage. $L_S\frac{di_d}{dt}$ and $L_S\frac{di_q}{dt}$ have significant effects on *d*-axis and *q*-axis voltages when power changes rapidly, as shown in Eq. (11). However, $L_S\frac{di_d}{dt}$ and $L_S\frac{di_q}{dt}$ increase the noise of the control system and reduce the

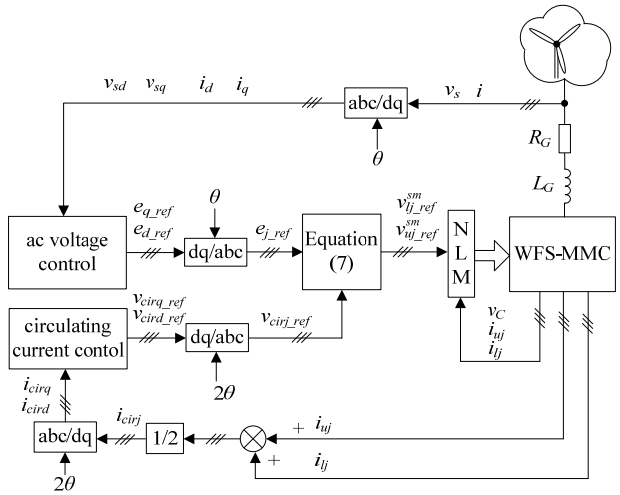

Fig. 3. Control of WFS-MMC.

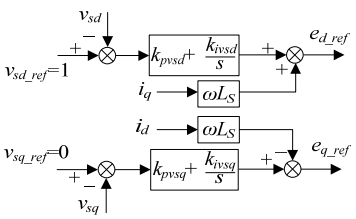

Fig. 4. AC voltage control based on PI controller.

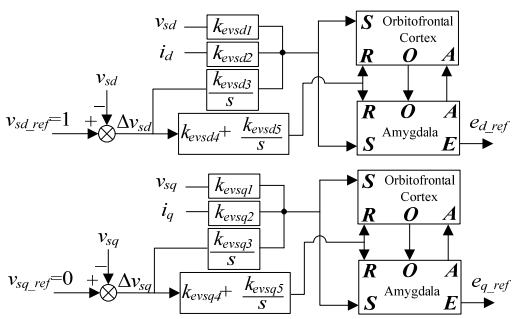

Fig. 5. AC voltage control based on an EL controller.

stability if they are directly used by the controller. The AC voltage control based on the traditional PI controller is designed as shown in Fig. 4, which does not include the terms $L_S \frac{di_d}{dt}$ and $L_S \frac{di_q}{dt}$.

In this section, a novel controller based on EL is designed to control the AC voltage, and its schematic is depicted in Fig. 5. Self-learning of the EL controller is beneficial for addressing problems caused by wind power randomness, system parameter variation, and rapid local load change.

The *S* refers to the elements that affect the inner EMF *e*. According to Eq. (11), *S* utilizes v_s and $\int \Delta v_s dt$; contains i_d and i_q for the *d*-axis and *q*-axis voltage controls respectively (Fig. 5). With the help of the EL mechanism, the proposed controller can consider the effects of i_d and i_q for the *d*-axis and *q*-axis voltage controls respectively. To reduce the

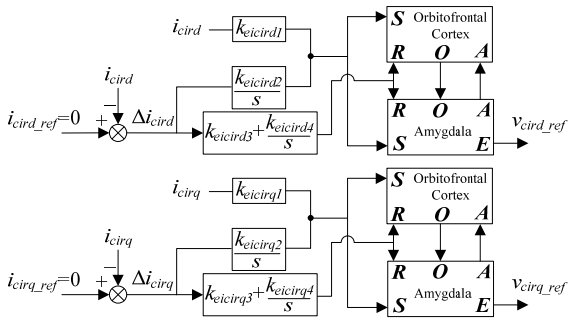

Fig. 6. Circulating current control based on an EL controller.

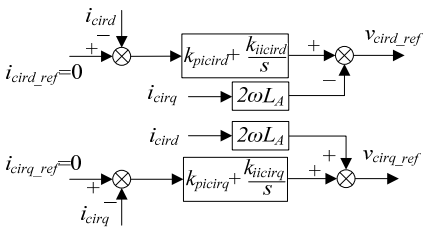

Fig. 7. Circulating current control based on a PI controller.

dimension of *S* and simplify the control structure, *S* does not include $\omega L_S i_q$ and $\omega L_S i_d$, which are regarded as disturbances for the controller. The functions of *S* for the *d*-axis and *q*-axis voltage controls are therefore set as Eqs. (21) and (22). *R* is defined to evaluate the control effect. The proportion of error can be used to describe the real-time control effect, and the error integral tends to describe the steady control effect. The proposed EL controller adopts the PI output as the role of *R*, as shown by Eqs. (23) and (24).

$$S_{vsd} = [k_{evsd1} v_{sd} \quad k_{evsd2} i_d \quad k_{evsd3} \int \Delta v_{sd} dt]^T \tag{21}$$

$$S_{vsq} = [k_{evsq1} v_{sq} \quad k_{evsq2} i_q \quad k_{evsq3} \int \Delta v_{sq} dt]^T \tag{22}$$

$$R_{vsd} = k_{evsd4} \Delta v_{sd} + k_{evsd5} \int \Delta v_{sd} dt \tag{23}$$

$$R_{vsq} = k_{evsq4} \Delta v_{sq} + k_{evsq5} \int \Delta v_{sq} dt \tag{24}$$

C. Circulating Current Control

i_{cirj} contains other frequency components besides the major component, namely, the double line-frequency. The learning mechanism decreases the noise sensitivity of the EL controller and helps suppress the circulating current. The use of the EL controller to control the circulating current is proposed in this article on the basis of Eq. (12). Similarly, for the design of AC voltage controller, the block diagram of the proposed EL controller for controlling the circulating current is shown in Fig. 6. The *S* and *R* of the EL circulating current controller are defined as Eqs. (25)–(28). The traditional PI controller for the circulating current control (Fig. 7) is provided for comparison of the effect between the EL and PI controllers.

$$S_{icird} = [k_{eicird1} i_{icird} \quad k_{eicird2} \int \Delta i_{cird} dt]^T \tag{25}$$

$$S_{icirq} = [k_{eicirq1} i_{icirq} \quad k_{eicirq2} \int \Delta i_{cirq} dt]^T \tag{26}$$

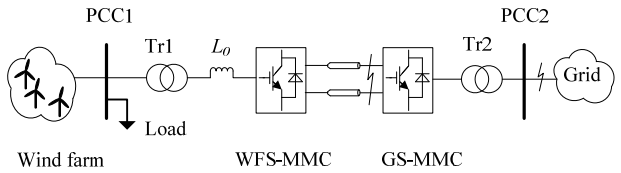

Fig. 8. MMC–HVDC system.

$$R_{icird} = k_{eicird3}\Delta i_{icird} + k_{eicird4}\int \Delta i_{icird}dt \quad (27)$$

$$R_{icirq} = k_{eicirq3}\Delta i_{icirq} + k_{eicirq4}\int \Delta i_{icirq}dt \quad (28)$$

IV. Simulation Results and Discussion

The system configuration under study (Fig. 8) is composed of an MMC–HVDC transmission system connected to a doubly fed induction generator (DFIG) wind farm. The MMC–HVDC system applies the parameters shown in Table I. GS–MMC operates in *VQ* mode, which maintains the DC voltage and controls the reactive power. The wind farm is modeled as a sum of an aggregated capacity of a single DFIG wind turbine with the parameters in Table II.

The parameters of the EL controller require tuning to achieve satisfactory performance. The learning of the amygdala is monotonous. Increasing α shortens the time the controller reaches the setting value in the transient process at the cost of stability. Meanwhile, increasing β decreases the steady error but worsens the dynamic performance. α is usually smaller than β for enhanced stability. The parameters of the EL controllers for the AC voltage and circulating current controls are given as Tables III and IV respectively.

The simulation results with traditional PI controllers for the AC voltage and circulating current controls (Figs. 4 and 7) are carried out to compare their control effects with those of the proposed EL controllers. The parameters of the PI controllers listed in Table V are obtained by trial and error to attain similar control responses.

The control performances are validated by four cases under different conditions. In all the simulations, the AC voltage of WFS–MMC and DC voltage of GS–MMC are controlled to reach the rated value. The reactive power of GS–MMC is maintained at 0 Mvar (unity power factor). The based values of the simulation results are shown as Table VI.

A. Case 1: Random Wind Speed and System Parameter Variation

Under the steady-state operation, random wind speed [Fig. 9(a)] is applied to illustrate the merits of the proposed EL controllers for AC voltage and circulating current controls. To show the performance of the EL controller during disturbance, an inductor L_0 with a random value from 0 to 0.1 mH [Fig. 9(b)] is connected in series between the wind farm and the WFS–MMC. The EL controller is also applied for the circulating current control. Fig. 9 shows the control performances of the AC voltage and circulating current controls. Simulation results of the traditional PI controllers with the same wind speed and L0 are depicted in Fig. 10. A comparison of Figs. 9 and 10 clearly reveals that the proposed EL controllers achieve more stable controls for the AC voltage and circulating current with less fluctuation than the PI controllers. The mean-square error (MSE) values [4],

TABLE I
Parameters of the MMC–HVDC System

Parameters	Values
Rated power of GS–MMC, WFS–MMC, Tr1, and Tr2	200 MVA
Rated frequency	50 Hz
Rated AC voltage of GS–MMC and WFS–MMC	175 kV
Rated DC-link voltage	320 kV
Rated AC voltage of PCC1 and PCC2	230 kV
Winding voltage of Tr1 and Tr1	230/175 kV
Leakage reactance of Tr1 and Tr2	0.1 p.u.
Arm inductance	50 mH
Capacitance of sub-module	3000 μF
Number of sub-modules in each arm	80
Length of cable	200 km
DC resistance of cable	0.03182 ohm/km

TABLE II
Parameters of DFIG

Parameters	Values
Rated power	200 MVA
Rated voltage	575 V
Rated frequency	50 Hz
Stator resistance	0.00706 p.u.
Rotor resistance	0.005 p.u.
State leakage inductance	0.171 p.u.
Rotor leakage inductance	0.156 p.u.
Magnetizing inductance	2.9 p.u.
Angular moment of inertia	2 s

TABLE III
Parameters of the EL Controller for AC Voltage Control

Parameters	Values	Parameters	Values
k_{evsd1}	0.8	k_{evsq1}	0.8
k_{evsd2}	1.5	k_{evsq2}	1.5
k_{evsd3}	2500	k_{evsq3}	2000
k_{evsd4}	15	k_{evsq4}	0.5
k_{evsd5}	2000	k_{evsq5}	500
α_{vsd}	0.0001	α_{vsq}	0.0001
β_{vsd}	0.001	β_{vsq}	0.0028

TABLE IV

PARAMETERS OF THE EL CONTROLLER FOR CIRCULATING CURRENT CONTROL

Parameters	Values	Parameters	Values
$k_{eicird1}$	1	$k_{eicirq1}$	1
$k_{eicird2}$	100	$k_{eicirq2}$	100
$k_{eicird3}$	50	$k_{eicirq3}$	50
$k_{eicird4}$	200	$k_{eicirq4}$	200
α_{icird}	0.001	α_{icirq}	0.001
β_{icird}	0.002	β_{icirq}	0.002

TABLE V

PARAMETERS OF THE PI CONTROLLERS FOR AC VOLTAGE AND CIRCULATING CURRENT CONTROLS

Parameters	Values	Parameters	Values
k_{pvsd}	0.2	k_{picird}	0.4
k_{ivsd}	2000	k_{iicrid}	250
k_{pvsq}	0.2	k_{picirq}	0.4
k_{ivsq}	2000	k_{iicirq}	250

TABLE VI

BASED VALUES OF THE SIMULATION RESULTS

Parameters	Values
Based active power	200 MW
Based reactive power	200 Mvar
Based DC-link voltage	320 kV
Based AC voltage at PCC1 and PCC2 (including in the dq frame)	187.794 kV
Based circulating current of WFS–MMC	0.933 kA

TABLE VII

MSE VALUES OF THE EL CONTROLLER AND THE PI CONTROLLER IN DIFFERENT CASES

Case	MSE	EL Controller	PI controller	Improvement Rate (%)
Case 1	MSE(v_{sd})	0.000010	0.000037	73.5
	MSE(v_{sq})	0.000047	0.000102	53.6
	MSE(i_{cird})	0.000021	0.000069	69.2
	MSE(i_{cirq})	0.000014	0.000070	80.0
Case 2	MSE(v_{sd})	0.000008	0.000019	55.8
	MSE(v_{sq})	0.000031	0.000045	31.9
Case 3	MSE(v_{sd})	0.000010	0.000037	72.7
	MSE(v_{sq})	0.000047	0.000103	54.5
Case 4	MSE(v_{sd})	0.000013	0.000066	79.9
	MSE(v_{sq})	0.000057	0.000123	53.7

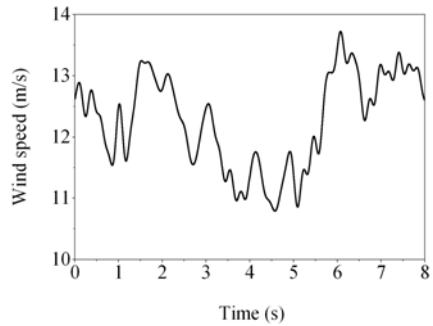

(a) Wind speed.

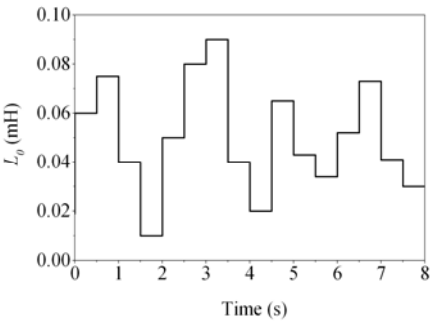

(b) L_0.

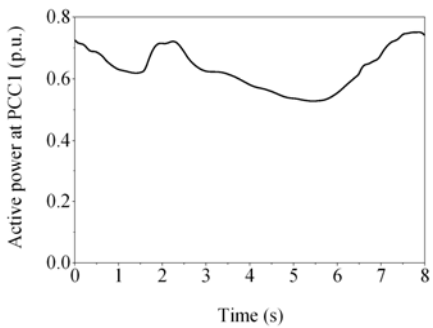

(c) Active power at PCC1.

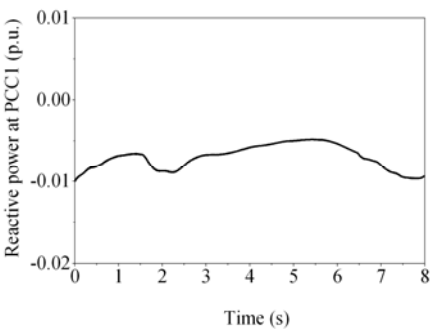

(d) Reactive power at PCC1.

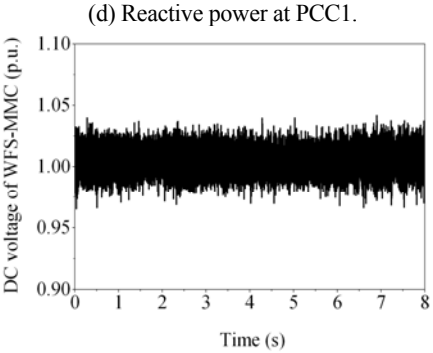

(e) DC voltage of WFS–MMC.

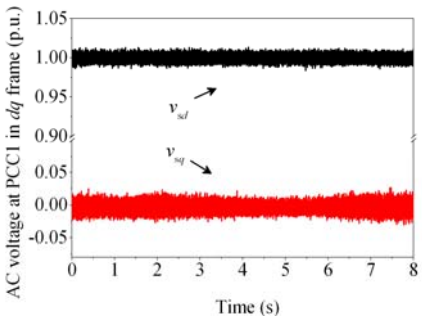

(f) AC voltage at PCC1 in *dq* frame.

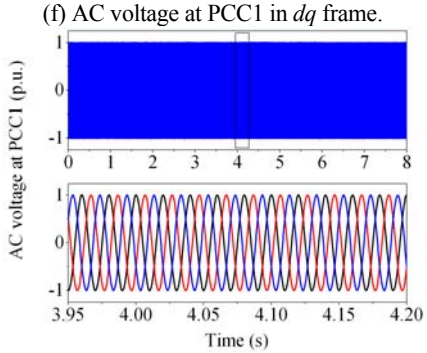

(g) AC voltage at PCC1.

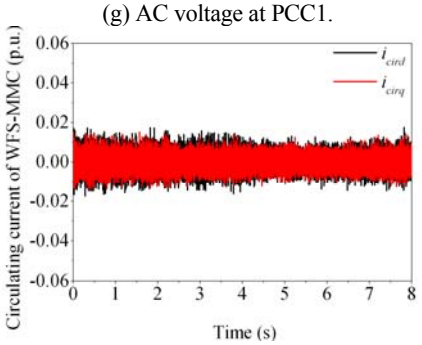

(h) Circulating current of WFS–MMC in the *dq* frame.

Fig. 9. Simulation results of EL controllers for AC voltage and circulating controls in Case 1.

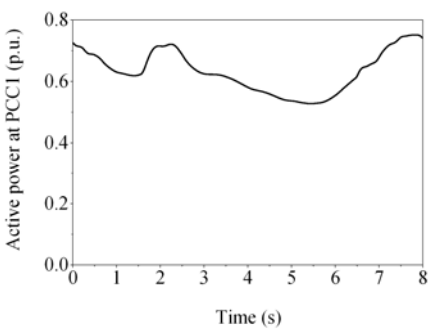

(a) Active power at PCC1.

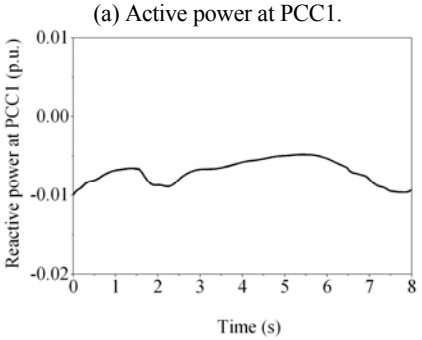

(b) Reactive power at PCC1.

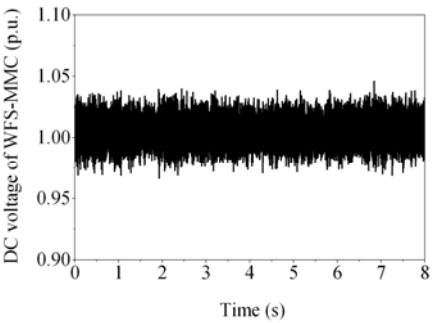

(c) DC voltage of WFS–MMC.

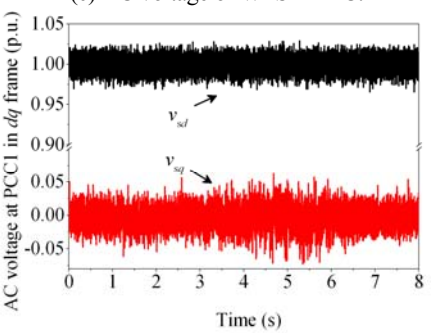

(d) AC voltage at PCC1 in the *dq* frame.

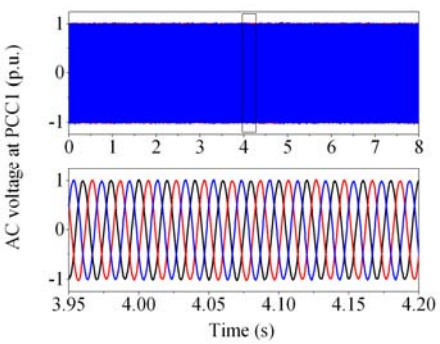

(e) AC voltage at PCC1.

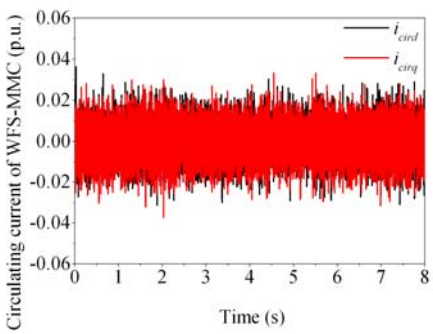

(f) Circulating current of WFS–MMC in the *dq* frame.

Fig. 10. Simulation results of PI controllers for the AC voltage and circulating controls in Case 1.

[21] of v_{sd}, v_{sq}, i_{cird}, and i_{cirq} improve 73.5%, 53.6%, 69.2%, and 80%, respectively, as shown in Table VII.

$$MSE(val) = \frac{1}{n}\sum_{i=1}^{n}(val_i - val_{ref})^2 \tag{29}$$

B. Case 2: Local Load Rapid Change

This case is similar to the case above, except that the local

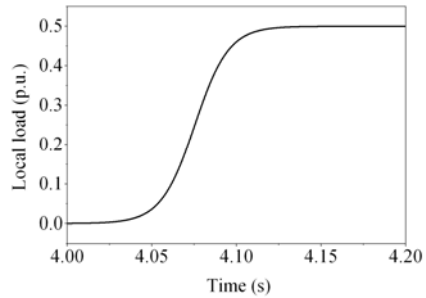

(a) Local load at PCC1.

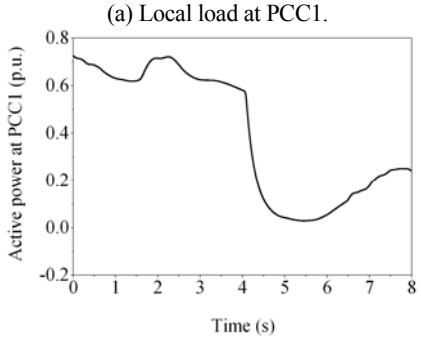

(b) Active power at PCC1.

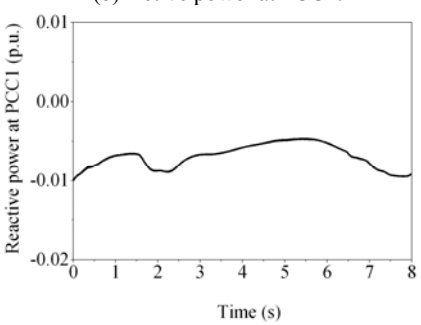

(c) Reactive power at PCC1.

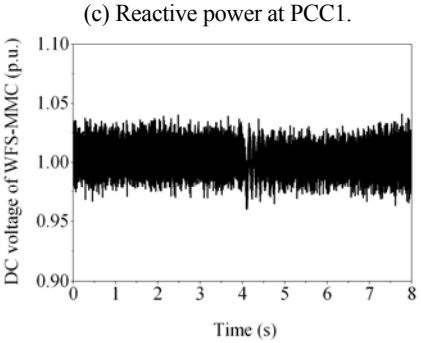

(d) DC voltage of WFS–MMC.

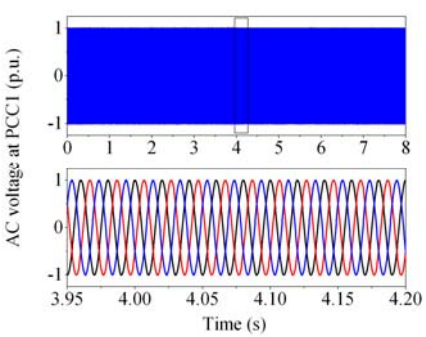

(e) AC voltage at PCC1.

Fig. 11. Simulation results of the EL controller for AC voltage control in Case 2.

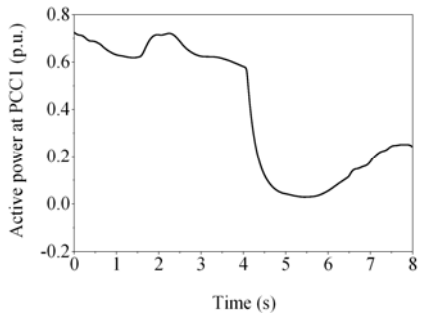

(a) Active power at PCC1.

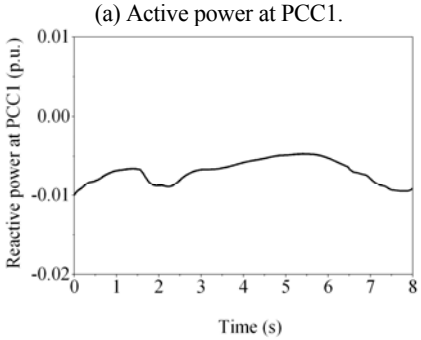

(b) Reactive power at PCC1.

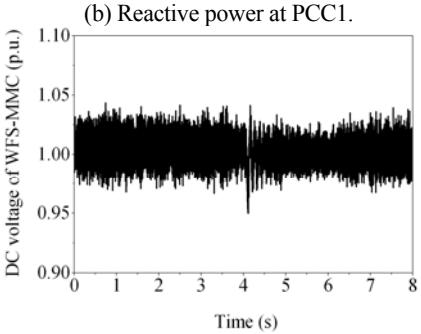

(c) DC voltage of WFS–MMC.

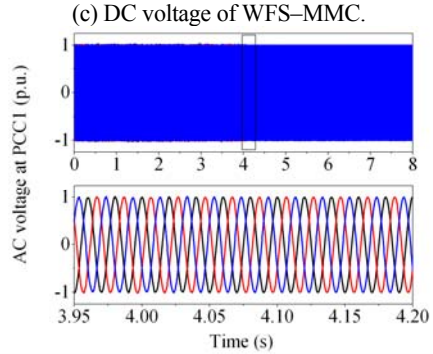

(d) AC voltage at PCC1.

Fig. 12. Simulation results of the EL controller for AC voltage control in Case 2.

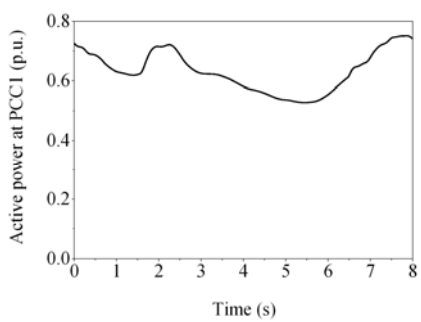

(a) Active power at PCC1.

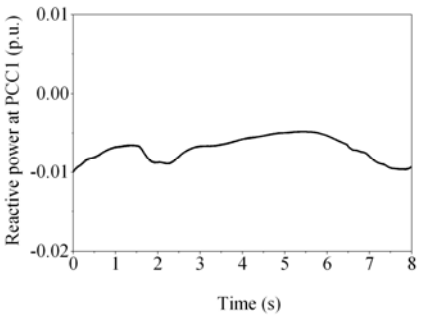

(b) Reactive power at PCC1.

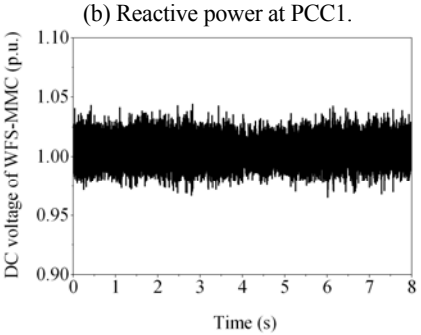

(c) DC voltage of WFS–MMC.

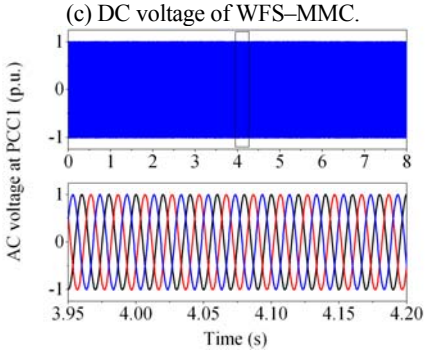

(d) AC voltage at PCC1.

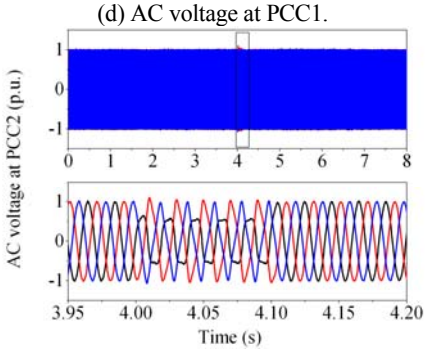

(e) AC voltage at PCC2.

Fig. 13. Simulation results of the EL controller for AC voltage control in Case 3.

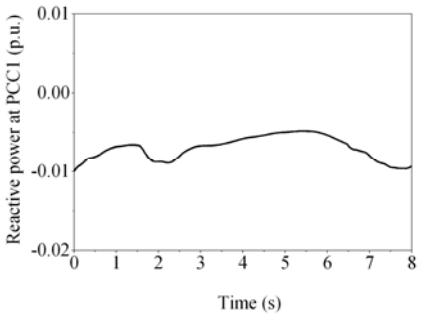

(b) Reactive power at PCC1.

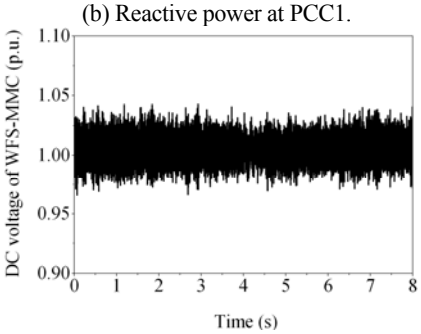

(c) DC voltage of WFS–MMC.

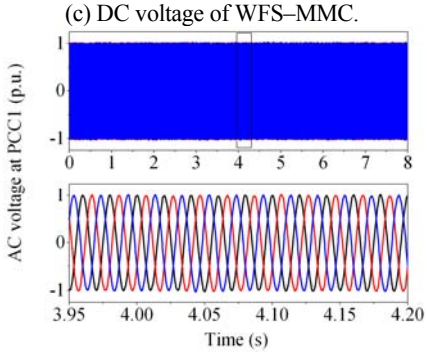

(d) DC voltage at PCC1.

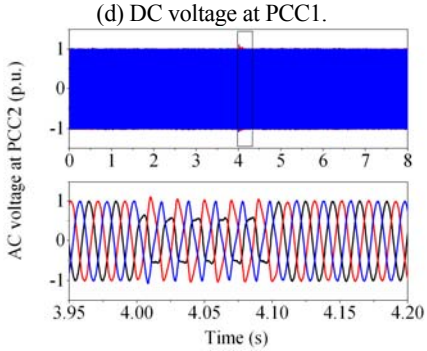

(e) AC voltage at PCC2.

Fig. 14. Simulation results of the PI controller for AC voltage control in Case 3.

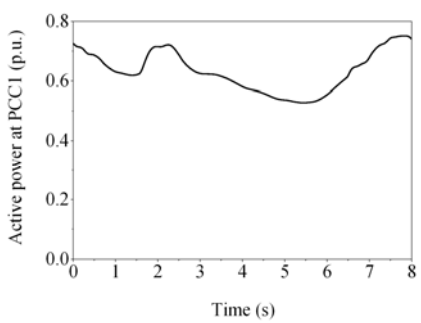

(a) Active power at PCC1.

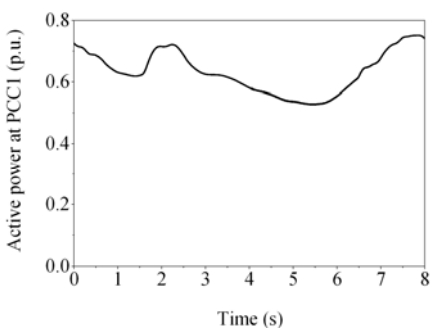

(a) Active power at PCC1.

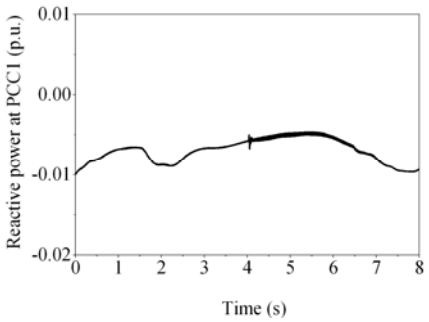

(b) Reactive power at PCC1.

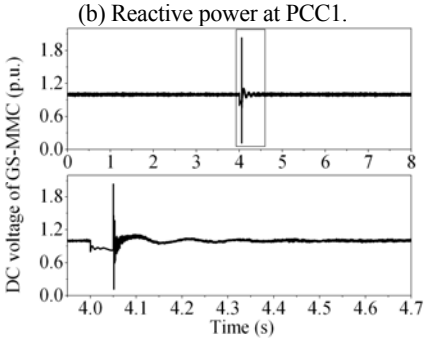

(c) DC voltage of GS–MMC.

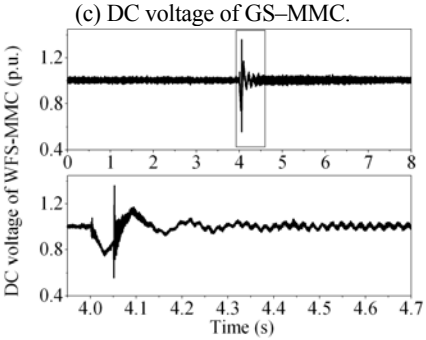

(d) DC voltage of WFS–MMC.

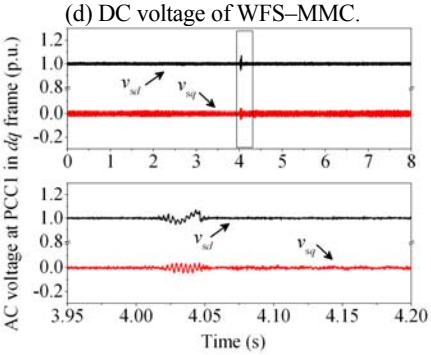

(e) AC voltage at PCC1 in the *dq* frame.

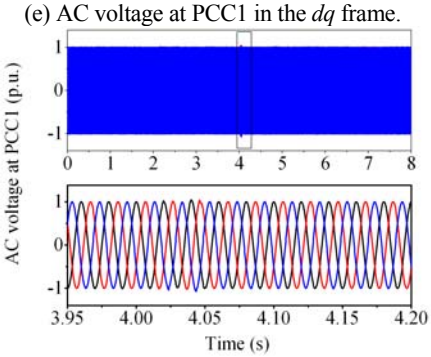

(f) AC voltage at PCC1.

Fig. 15. Simulation results of the EL controller for AC voltage control in Case 4.

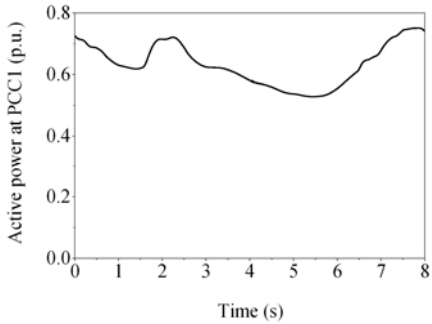

(a) Active power at PCC1.

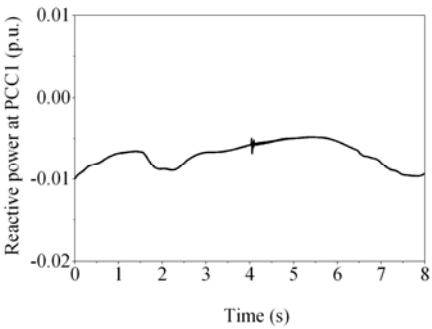

(b) Reactive power at PCC1.

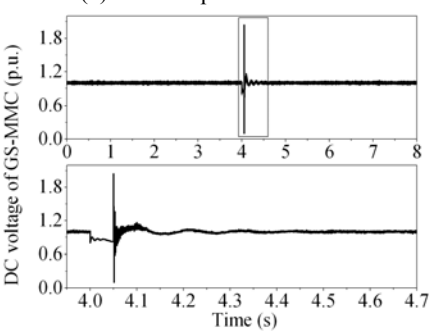

(c) DC voltage of GS–MMC.

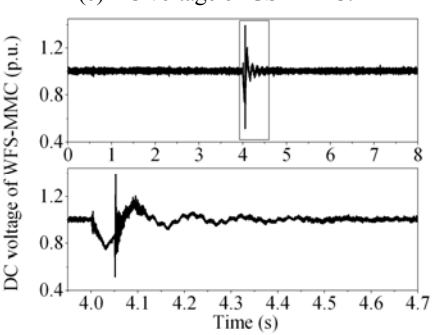

(d) DC voltage of WFS–MMC.

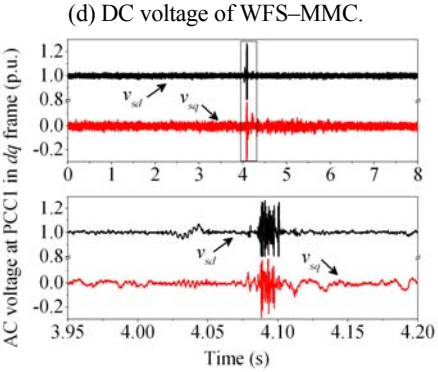

(e) AC voltage at PCC1 in the *dq* frame.

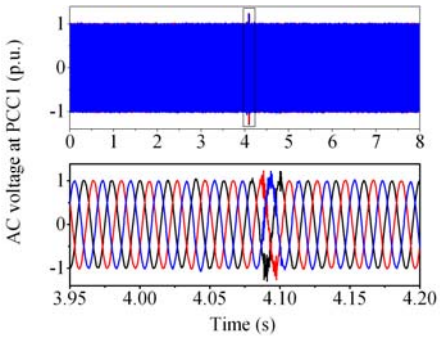

(f) ac voltage at PCC1.

Fig. 16. Simulation results of the PI controller for AC voltage control in Case 4.

load at PCC1 rapidly changes from 0 MW to 100 MW (0.5 p.u.) as shown in Fig. 11(a), and no L_0 is included. The simulation results in Figs. 11 and 12 show that the proposed EL controller provides more stable control with less effect on the DC voltage than the traditional PI controller. The respective maximum and minimum of DC-link voltage are 1.0367 and 0.9604 p.u. for the EL controller when the local load rapidly changes, and 1.0413 and 0.9501 p.u. for the traditional PI controller. As shown in Figs. 11(e) and 12(e), the rapid change did not significantly influence the AC voltages for both controllers.

C. Case 3: AC Voltage Fault in the Grid Side

In this case, a single-phase voltage sag at PCC2 with a magnitude of 0.5 p.u. and a duration of 100 ms is implemented to show the transient behavior of the AC voltage control during a major system fault. Figs. 13 and 14 give the simulation results based on the EL and PI controllers in this case. Figs. 13(d) and 14(d) show that no significant distortion exists in the AC voltage during the fault in the grid side.

D. Case 4: DC Voltage Sag at GS–MMC

The AC fault in the previous section is blocked by the DC link and slightly affects the WFS–MMC. In this case, a DC voltage sag at GS–MMC with a magnitude of 0.2 p.u. and a duration of 50 ms is implemented to show the transient behavior of the AC voltage control during the DC voltage fault. The influence of the DC voltage sag on WFS–MMC is directly related to the AC voltage. Given Eq. (11), $L_S \frac{di_d}{dt}$ and $L_S \frac{di_q}{dt}$ significantly affect the AC voltage in the transient process. A comparison of Figs. 15 and 16 reveal that the proposed controller offers superior performance with much smaller fluctuation in the transient process. For the EL controller, v_{sd} lies in [0.9468 p.u., 1.0691 p.u.] and v_{sq} lies in [−0.0481 p.u., 0.0382 p.u.]; for the PI controller, the values are [0.7294 p.u., 1.2685 p.u.] and [−0.2840 p.u., 0.2284 p.u.] respectively.

V. Conclusions

The major contributions of this study are the successful construction of novel EL controllers for AC voltage and circulating current controls based on the EL in amygdala and orbitofrontal cortex, as well as the consideration of the *d*-axis and *q*-axis currents on *d*-axis and *q*-axis voltage controls respectively to improve the AC voltage control effect. The effectiveness of the proposed controllers is confirmed under different conditions in comparison with traditional PI controllers. The MSE values in Table VII show that the proposed controllers significantly improve the four cases. Particularly, for the DC voltage sags at GS–MMC, v_{sd} and v_{sq} fluctuated much less than those of the PI controller.

Acknowledgment

This research was supported by the Scientific Research Foundation of State Key Laboratory of Power Transmission Equipment and System Security (2007DA10512713303).

References

[1] L. Wang and M. S. N. Thi, "Comparative stability analysis of offshore wind and marine-current farms feeding into a power grid using HVDC links and HVAC line," *IEEE Trans. Power Del.*, Vol. 28, No. 4, pp. 2162-2171, Oct. 2013.

[2] J. L. Sawin, E. Martinot, D. Barnes, A. McCrone, J. Roussell, R. Sims, V. S. O'Brian, R. Adib, J. Skeen, E. Musolino, L. Riahi, and L. Mastny, "Renewables 2011: global status report," *Renewable Energy Policy Network for the 21st Century*, Vol. 46, No. 38, p. 116, 2011.

[3] "Global wind statistics 2014," *GWEC*, pp. 1-4, 2015.

[4] G.-D. Wang, R.-J. Wai, and Y. Liao, "Design of backstepping power control for grid-side converter of voltage source converter-based high-voltage dc wind power generation system," *IET Renewable Power Generation*, Vol. 7, No. 2, pp. 118-133, Mar. 2013.

[5] S. Cole and R. Belmans, "Transmission of bulk power," *IEEE Ind. Electron. Mag.* Vol. 3, No. 3, pp. 19-24, Sep. 2009.

[6] N. Flourentzou, V. G. Agelidis, and G. D. Demetriades, "VSC-based HVDC power transmission systems: an overview," *IEEE Trans. Power Electron.*, Vol. 24, No. 3, pp. 592-602, Mar. 2009.

[7] J. Pan, R. Nuqui, K. Srivastava, T. Jonsson, P. Holmberg, and Y. J. Hafner, "AC grid with embedded VSC-HVDC for secure and efficient power delivery," in *IEEE Energy 2030 Conference*, pp. 1-6, Nov. 2008.

[8] R. E. Torres-Olguin, A. Garces, M. Molinas, and T. Undeland, "Integration of offshore wind farm using a hybrid HVDC transmission composed by the PWM current-source converter and line-commutated converter," *IEEE Trans. Energy Convers.*, Vol. 28, No. 1, pp. 125-134, Mar. 2013.

[9] N. Ahmed, L. Angquist, S. Norrga, A. Antonopoulos, L. Harnefors, and H. P. Nee, "A computationally efficient continuous model for the modular multilevel converter," *IEEE J. Emerg. Sel. Topics Power Electron.*, Vol. 2, No. 4, pp. 1139-1148, Dec. 2014.

[10] A. Lesnicar and R. Marquardt, "An innovative modular multilevel converter topology suitable for a wide power range," in *IEEE Bologna Power Tech Conference Proceedings*, pp. 1-6, Jun. 2003.
[11] B. Gemmell, J. Dorn, D. Retzmann, and D. Soerangr, "Prospects of multilevel VSC technologies for power transmission," in *IEEE/PES Transmission and Distribution Conference and Exposition*, pp. 1-16, Apr. 2008.
[12] S. Debnath, J. Qin, B. Bahrani, M. Saeedifard, and P. Barbosa, "Operation, control, and applications of the modular multilevel converter: a review," *IEEE Trans. Power Electron.*, Vol. 30, No. 1, pp. 37-53, Jan. 2015.
[13] L. Xu, L. Yao, and C. Sasse, "Grid integration of large DFIG-based wind farms using VSC transmission," *IEEE Trans. Power Syst.*, Vol. 22, No. 3, pp. 976-984, Aug. 2007.
[14] L. Guan, X. Fan, Y. Liu, and Q.H. Wu, "Dual-mode control of AC/VSC-HVDC hybrid transmission systems with wind power integrated," *IEEE Trans. Power Del.*, Vol. 30, No. 4, pp. 1686-1693, Aug. 2015.
[15] Q. Tu, Z. Xu, and L. Xu, "Reduced switching-frequency modulation and circulating current suppression for modular multilevel converters," *IEEE Trans. Power Del.*, Vol. 26, No. 3, pp. 2009-2017, Jul. 2011.
[16] S. Rohner, S. Bernet, M. Hiller, and R. Sommer, "Analysis and simulation of a 6 kV, 6 MVA modular multilevel converter," in *35th Annual Conference of IEEE Industrial Electronics*, pp. 225-230, 2009.
[17] Q. Song, W. Liu, X. Li, H. Rao, S. Xu, and L. Li, "A steady-state analysis method for a modular multilevel converter," *IEEE Trans. Power Electron.*, Vol. 28, No. 8, pp. 3702-3713, Aug. 2013.
[18] X. She, A. Huang, X. Ni, and R. Burgos, "AC circulating currents suppression in modular multilevel converter," in *38th Annual Conference on IEEE Industrial Electronics Society(IECON)*, pp. 191-196, Oct. 2012.
[19] J. Moren, *Emotion and learning - a computational model of the amygdala*, Ph.D. Dissertation, Lund University, Sweden, 2002.
[20] M. A. Rahman, R. M. Milasi, C. Lucas, B. N. Araabi, and T. S. Radwan, "Implementation of emotional controller for interior permanent-magnet synchronous motor drive," *IEEE Trans. Ind. Appl.*, Vol. 44, No. 5, pp. 1466-1476, Sep./Oct. 2008.
[21] S. M. Kay, "Fundamentals of statistical signal processing," *Prentice Hall PTR*, Chapter 2, pp. 19-20, 1993.

Keli Li was born in Guangxi, China, in 1984. He received his B.S. degree from Nanchang University, China, in 2008, and his M.S. degree from Chongqing University of Technology, China, in 2011. He is currently working toward his Ph.D. in Electrical Engineering degree in Chongqing University, China. His current research interests include the application of VSC-HVDC, multilevel converters, and grid integration of renewable energy.

Yong Liao received his M.Eng. degree in Electrical Machinery and his Ph.D. degree in Power System Control from Chongqing University, Chongqing, China, in 1988 and 1997 respectively. He is currently a Professor of Electrical Machinery and Apparatus at Chongqing University. His research interests include VSC–HVDC and the control of doubly fed electrical machines as used in renewable energy systems, including wind and micro-hydro generators. In 1998, he participated in the Global Development Programme of Rockwell Automation, Milwaukee, WI. From 2001 to 2002, he was a Visiting Professor at Northumbria University, Newcastle, U.K.

Ren Liu received his M.Eng. and Ph.D. degrees in Electrical Engineering from Chongqing University, Chongqing, China, in 2004 and 2008 respectively. He is currently a lecturer of electrical machinery and apparatus at Chongqing University. His research interests include renewable energy and control of electrical machines.

Jimiao Zhang received his B.Eng degree in Computer Engineering from Guangdong University of Foreign Studies, Guangzhou, China, in 2012 and his M.Eng degree in Electrical Engineering from Chongqing University, Chongqing, China, in 2015. His research interests include AC motor drive system and power electronics.